A POTENTIAL OF POLARIMETRIC SAR DATA IN MAPPING FIRST YEAR SEA ICE PRESSURE RIDGES FROM THE COHERENT AND NON-COHERENT COMPONENTS OF *HH* AND *VV* CHANNELS

Eric Hudier[1] and Pierre Larouche[2]

1. Université du Québec à Rimouski, Département de Mathématiques, d'Informatique et de Génie, Rimouski (Qc.), Canada G5L 3A1; eric_hudier(at)uqar.qc.ca
2. Institut Maurice-Lamontagne, Remote Sensing Laboratory, Mont-Joli (Qc.), Canada G5H 3Z4; larouchep(at)dfo-mpo.gc.ca

ABSTRACT

During the early melt period, the air-ice and air-snow temperature conditions may vary from melting to freezing within 12 hours. When solar irradiance and air temperature are at their maximum, the increased wetness of the snow layer coupled with the development of a liquid film on exposed ice faces increases the contrast between ridges and flat ice areas. We present two images recorded at 4 am and 4 pm that show this natural enhancement process of ridges when a liquid phase is present on ice blocks (4 pm). Besides, it also shows that, on the contrary, the development of new ice crystals during the night create conditions that highly reduce the contrast between ridges and flat ice areas (4 am image).

For smooth wet surfaces the backscattering at normal incidence is dominated by the coherent component. In addition, the non-coherent component is maximum at normal incidence. The variability in surface slope orientations being a characteristic of ridge areas, we computed probability densities that pixels from ridge regions would be identified as ridge pixels. Both coherent and non-coherent models show a dependence on block size and the applied threshold value. As anticipated, the coherent model gives the highest probability levels with a maximum for cubic blocks of 0.4 m. The maximum value with non-coherent backscattering is reached for 1 m blocks.

Keywords: Ice, ridge, SAR

INTRODUCTION

Pressure ridges result from the deformation of the ice under the stress that develops from combined effects of wind and currents. They form linear structures of piled ice blocks at the border of un-deformed ice plates. In our study area, we measured sails up to 5 m in height and density between 1.9 to 4.1 ridges per km (1). According to Lytle et Ackley (2) ridges and rubble fields may account for up to 30% of the ice surface and up to 50% of the total ice mass (3,4,5) with densities of up to 20 ridges/kilometre (6,7).

Snow-covered sea ice is an important component of high-latitude environments. It forms an uneven solid interface that separates the ocean from the atmosphere and therefore controls fluxes between the two mediums (8). A number of models have been developed to describe ocean-atmosphere exchanges as much as to study the oceanic and atmospheric circulation under and above the ice cover. Beside numerous difficulties that result from modelling a multi-roughness scale boundary layer, researchers are constrained by the lack of statistical data that describe the distribution and characteristics of ridges.

In the remote sensing literature, first-year ridges are described as bright linear structures, with strong backscattering associated with tilted blocks (9,10). To better explore this observation surface scattering models separate the coherent σ^o_{coh} from the non-coherent σ^o_N components:

$$\sigma^o_{ff} = \sigma^o_{coh} + \sigma^o_N$$

The diffuse non-coherent component of the surface backscattered signal is a function of the dielectric discontinuity between the two mediums, the roughness statistics of the interface and the SAR beam incident angle. The dependence of the backscattered field with the incidence angle is of interest in the way that it links the data with the physical distribution of the ice block's orientation and snow surface slope in the ridge environment. At this point, it is pertinent for the reader's benefit to underline that incidence angles are defined with respect to the area of study whatever its size. Meaning that the incidence angle relative to the face on an ice block should not be confused with the incidence angle relative to the scene.

At close to normal incidence, for very smooth surfaces, the phase structure may be preserved and the SAR beam's return hold a large coherent component, that, if filtered from speckle, can be used to pinpoint a ridge location. It is to be noted that in polarimetric data sets, the specular reflection that induces coherent signals results in $\sigma^o_{HH} \approx \sigma^o_{VV}$.

The speckle issue is of utmost importance for ridges. Extending only over several meters across, ridges are best resolved at the highest available resolution. However, the reduction of speckle is first achieved through simultaneous processing of multiple looks at the expense of spatial resolution. In fact, any attempt at getting information on ridges is hindered by the difficulties in extracting the very location of individual ridges out of a speckled image.

THE SPRING MELT ENHANCEMENT

The backscattered electric field is a sum of contributions from snow-air interface surface scattering (A), snow layer volume scattering (B), snow-ice interface surface scattering (C) and sea ice volume scattering (D) (11):

$$\sigma^o = \sigma^o_A + \sigma^o_B + \sigma^o_C + \sigma^o_D$$

The microwave signature of sea ice changes dramatically with the thermodynamic seasonal changes (9). During the winter season, the snow is dry, almost transparent to SAR frequencies, therefore image patterns reveal varying characteristics of the ice body properties or of the ice-snow interface. Under these conditions, the large number of unknowns makes ridge extraction unreliable.

By early spring, as melting starts and snow wetness increases, the snow-air interface scatters a large fraction of the incident SAR beam (mainly as forward-scattering). Over 8% water content, the transmitted component becomes negligible (12). This applies a natural mask over everything that is buried and magnifies the contribution of structures that emerge from the snow layer. The electromagnetic wave interaction with the interface discontinuity is then determined by the scattering efficiency of the surface roughness elements' shape (13,14,15).

This is well illustrated by the difference of contrast observed on ascending and descending orbits Radarsat 1 images recorded on April 26 and 29, 2001 (Figure 1). During the day, melting at the interface develops a liquid film that enhances forward scattering. Early in the morning, after freezing occurred during the night, newly formed crystals increase *rms* height and in turn result in a higher backscattering coefficient. The physics of the phenomenon being independent of the wave polarization, the same conclusion should apply to *HH* and *VV* polarization.

The analyses in the present paper are realized from nine Radarsat 1 fine beam mode (Table 1) and two first year sea ice SIR-C single look images. Radarsat images were obtained from a consolidated, thick (1.5m) first year sea ice located offshore Kuujjuarapik, Hudson Bay, Canada. In this region, early melt conditions are usually met by late April, or early May. On the table below, an (*) identifies images acquired when a liquid film was observed on ice blocks, and the averaged snow wetness measured on sites selected in the middle of un-deformed ice plates was over 6% in at least 80% of the samples. Polarimetric SIR-C images were recorded on April 1994 in the Gulf of St-Lawrence.

Table 1. Radarsat 1 images.

Recording date	Incidence angle	Orbit
April 4, 1998	36.8-39.9	Ascending
April 11, 1998	36.8-39.9	Descending
April 28, 1998 (*)	36.8-39.9	Ascending
May 5, 1998	36.8-39.9	Descending
March 26, 2001	36.8-39.9	Descending
April, 26 2001	40.3-42.5	Descending
April, 29 2001 (*)	41.1-43.1	Ascending

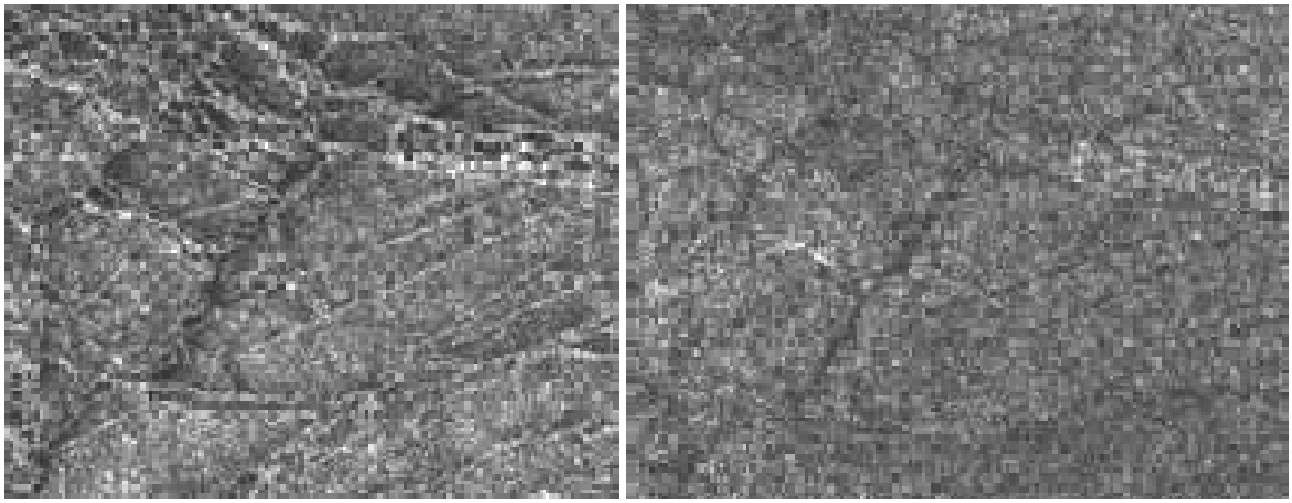

a) Ascending orbit; 16:00 local time b) Descending orbit; 4:00 local time

Figure 1: Radarsat 1 images of the same scene: a) at the end of a sunny day when the snow and ice surfaces were covered with a wet film, b) early in the morning after snow and ice wet films had turned into ice crystals.

THE POLARIMETRIC SAR FEATURES

The incidence angle dependence

Radar polarimeters measure the dimensional complex scattering matrix **S** from an area of the earth's surface. It relates the incident electric field E_i to the scattered field E_S (16):

$$\begin{bmatrix} E_{SH} \\ E_{SV} \end{bmatrix} = \frac{e^{ikr}}{r} \mathbf{S} \begin{bmatrix} E_{i1} \\ E_{i2} \end{bmatrix} = \frac{e^{ikr}}{r} \begin{bmatrix} S_{HH} & S_{HV} \\ S_{VH} & S_{VV} \end{bmatrix} \begin{bmatrix} E_{i1} \\ E_{i2} \end{bmatrix}$$

The subscripts *V* and *H* refer to horizontal and vertical polarization, *k* is the wavenumber and *r* is the distance between the radar antenna and the surface scattering area. In much of the literature on radar polarimetry, scattering symmetry is assumed: $S_{HV} = S_{VH}$ (17). It is more common to use the radar cross sections σ, and normalized radar cross section σ^o instead of the **S** matrix.

$$\sigma^o_{HH} = \left\langle S_{HH} S^*_{HH} \right\rangle_N \qquad \sigma^o_{VV} = \left\langle S_{VV} S^*_{VV} \right\rangle_N$$

$$\sigma^o_{HV} = \left\langle S_{HV} S^*_{HV} \right\rangle_N \qquad \sigma^o_{VH} = \left\langle S_{VH} S^*_{VH} \right\rangle_N$$

where $\langle \ \rangle_N$ stands for an *N* statistical looks average and S^* is the complex conjugate of *S*.

At close to normal incidence, which is the domain that applies to ridge extraction, $\sigma^o_{HH} = \sigma^o_{VV}$ for both the coherent and non-coherent components. For incidence angles larger than 10 to 20° the coherent component is negligible and it is necessary to consider separately smooth and rough surfaces. Rough surfaces exhibit a gentle decrease of the backscattering coefficient with little difference between σ^o_{HH} and σ^o_{VV}. With smooth surfaces σ^o_{HH} and σ^o_{VV} diverge as the incidence angle increases (9). The main difference with rough surfaces is a strong decrease of the backscattered energy in the 10 to 30° range. This property is of great value for the ridge extraction problem as it increases sharply the contrast between flat ice and regions in which tilted surfaces are found.

Several theoretical models provide expressions that, if not in total agreement with experimental data, give a realistic representation of the angular dependence of the co-polarized backscattering coefficients. After Ulaby et al. (18), the non-coherent backscattering component, for smooth surfaces characterized by a Gaussian autocorrelation function, is best modelled by the small perturbation method (SPM) expression:

$$\sigma^o_N = 4k^4 s^2 l^2 \cos^4\theta \left|\alpha(\theta,\varepsilon)\right|^2 \exp\left(-(kl\sin\theta)^2\right)$$

where *k*, *l*, *s* and $\alpha(\theta,\varepsilon)$ are the wavenumber, the surface correlation length, the *rms* surface height and the reflectivity factor for the SPM (for more details see Fung (19)); This expression will be used below to describe the diffused scattering in the non-coherent probabilistic model.

Specular coherent backscattering is achieved when the phase shift of the reflected wave is less than π. For slightly rough surfaces the coherent backscattering is given by Fung and Eom (20):

$$\sigma^o_{coh} = \frac{\left|\Gamma(\theta)\right|^2}{\beta^2} \exp\left(-4k^2 s^2 - \frac{\theta^2}{\beta^2}\right) \qquad (1)$$

where $\left|\Gamma(\theta)\right|$ is the Fresnel reflection coefficient, *s* the *rms* surface height, β the beam width and θ the incidence angle.

The speckle issue

Speckle is caused by the mutual coherence of returned wave fields. In the ridge extraction problem, speckle is often confused with other texture sources that induce variability in the backscattering from un-deformed ice plates. When the snow is wet and surface scattering is the only significant source in the signal, one can identify three elements in a signal:

$$\sigma^o_{pp} = \sigma^o_{pp,1} + \sigma^o_{pp,2} + \sigma^o_{pp,3}$$

where subscript (1) denotes fully developed speckle, (2) denotes point targets, and $\theta \cong 0°$ faces coherent returns, and (3) denotes non-coherent backscattering at close to normal incidence; *p* may be *H* or *V*.

The last two are not speckle; they result from snow cover slope variability and minor ice structures remnants from the consolidation period. The strength of the signal lies on the same principles that allow ridge extraction. The differentiation of coherent (2) and non-coherent (3) at close to normal incidence should then explore the differences in the statistics of this variability which will be discussed in the last section of this paper.

Fully developed speckle refers to the statistically Gaussian independence of the real and imaginary complex sums of electric fields backscattered from a given target (21). If the data acquisition was performed a second time under the same conditions, the same speckle should be observed. This coherence, unlike the smooth surface – normal incidence coherence (point targets), results from the geometry of the interface *at the order of the wavelength scale*. From geometric considerations it follows that it exists only for a given wave frequency and plane of propagation, which in turn implies that the vertical and horizontal signals are independent. Consequently, speckle induced bright pixels should not correlate on the *HH* and *VV* channels.

Under the Gaussian scatterer assumption, in a single-look image, the backscattering coefficient has an exponential probability distribution function (*Pdf*). Then, the probability that a given pixel value *X* may be over a certain threshold value *R* and an average return *B* over an un-deformed ice area is given by

$$Pdf(X > R) = \exp(-R/B).$$

It follows that the probability speckle generates a pixel value over the threshold *R* on both *HH* and *VV* data sets is $(Pdf(X > R))^2$, i.e. a reduction of speckle by a factor of $(1 - Pdf(X > R))$.

Computing the averaged values for *R* and *B* from the April 29, 2001 Radarsat 1 image (*R* = -12dB and *B* = -15dB) we obtain a residual 15% of the plate pixels with brighter returns than the threshold. This is consistent with the 13.5% that is predicted by the model for a perfect Gaussian distribution of scatterers. The difference can be explained by surface variability within the sampled sites. Applying the same method on the *HH* and *VV* SIR-C images we got 17% and 19% brighter pixels than the threshold on the selected un-deformed test area. Keeping only the pixel values that are over the threshold on both *HH* and *VV* this number reduces to 3% of the test area's pixels or a 83% reduction, all of them in ridged areas.

THE PROBABILISTIC MODEL

In satellite images, ridge detection results from the occurrence of snow or ice surfaces the backscatter of which is higher than the background. This is in turn linked to the degree of variability in snow and ice surface orientations in these structures. The higher the range of incidence angles, the greater are the odds that one of the faces is almost normal to the incident beam. It should be pointed out that, in the following, incidence angles will be determined relative to individual blocks, meaning that over a given area a range of incident angles may have to be considered.

A scene can be modelled as an ensemble of "homogenous" sub-scenes, homogenous meaning that the characteristics that control scattering are constant over the corresponding area. When only non-coherent signals are backscattered by each of the sub-scenes, the total backscatter is proportional to the sum of all cross sections:

$$\left|E_{total}\right|^2 = \sum \left|E_{sub-scene}\right|^2,$$

where *E* is the electric field (22,23). This still applies when only one sub-scene backscatters a coherent signal. When two or more independent coherent signals are backscattered, the resultant electric field is a vector sum which in turn induces fading.

Coherent extraction probability

The probability of detecting a ridge from its coherent backscattering can be estimated by computing the odds that a single block is oriented so as one of its faces backscatters a signal over the threshold set for ridge extraction. Using Fung and Eom's (20) expression for the coherent backscattering (Eq. 1) and setting the threshold of extraction of a ridge pixel at $\sigma^o_{th} = -12dB$, we can calculate the relation between a block size and the maximum incidence angle at which its coherent backscattered signal would be over the threshold (Figure 2).

Then the probability that the pixel will be identified as a ridge pixel is given by (Figure 3):

$$P_{coh} = P(\theta)(1 - P(\theta))^{N-1} N$$

where $P(\theta)$ is the probability that one face of a block be oriented in the right range of angle and *N* is the number of blocks that can cover the illuminated area.

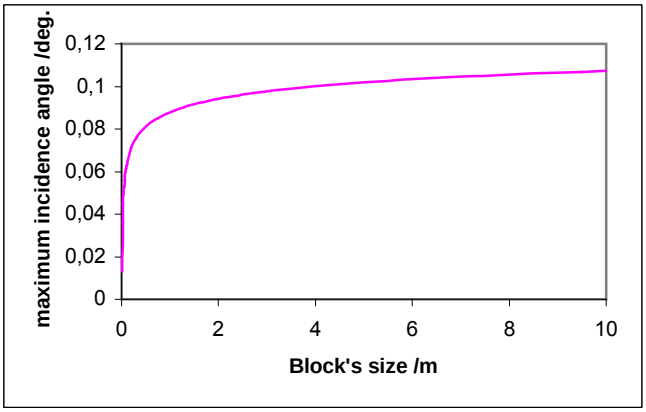

Figure 2: Relation incidence angle versus ice block's size for a pixel to be identified as a ridge pixel from coherent backscattering.

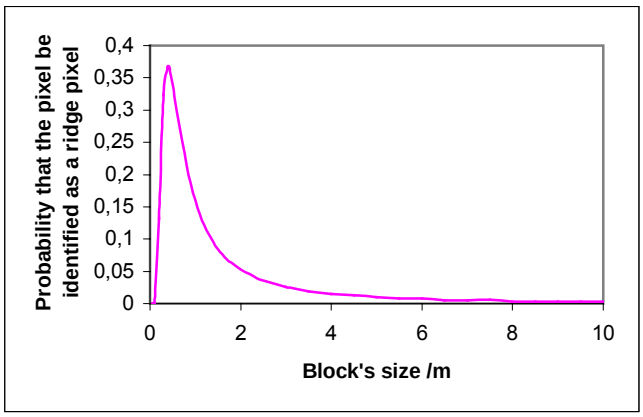

Figure 3: Probability that one and only one block is oriented in the range of incidence angles that would generate a coherent signal identifying the pixel as a ridge pixel.

Non-Coherent extraction probability

The incidence angle variability in ridges translates into a higher mean return than from plates. As a consequence, the probability that a pixel be over the threshold of detection is higher than in undeformed ice regions. Now, modelling the variability as a function of the number of blocks that are illuminated to define a pixel, one can compute the probability that a pixel will be identified as a ridge (24). This supposes that the whole *IFOV* is covered by identical blocks. The number of blocks is defined as the maximum number that could fit into the area represented by a pixel. Figure 4 shows the probability that the sum of the contributions of each of the N blocks simultaneously illuminated by the beam to form a pixel will be over the threshold of extraction on both *HH* and *VV* sets.

Beside the differences in the coherent and non-coherent formulations of the backscattering coefficient, the first model simulates the probability that one and only one block returns a coherent signal, while the second one computes the probability that the sum of the contributions of all the blocks register over the threshold. We observe that the maximum probability is reached for a cubic block of 0.4 m in the coherent model and 1 m in the non-coherent one. We observe that these optimums are dependent upon the value of the threshold used in the simulations. It results that applying a set of thresholds may allow us to obtain information on the average size of ice-blocks in a ridge. Furthermore, since this characteristic is a function of the thickness of the ice at the time the ridge was formed, it could hold some potential in ice thickness extraction which we are still unable to acquire from satellite images.

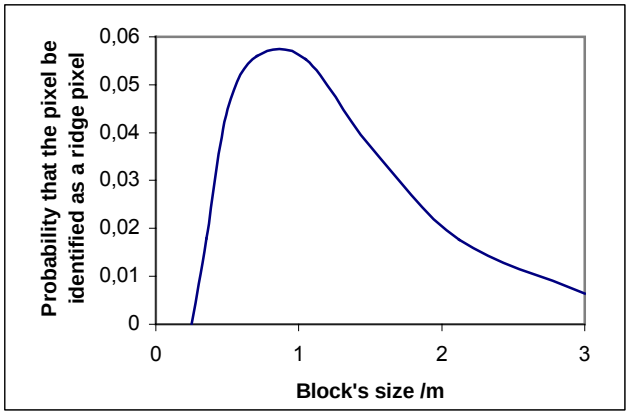

Figure 4: Probability for a pixel from an area of randomly oriented blocks of identical size to be identified as a ridge-pixel on both HH and VV polarisations.

CONCLUSIONS

The value recorded by a SAR for any given ground location is computed from the resultant backscattered electric field and, as a consequence, the sum of several contributions. By early spring, when snow wetness increases, it becomes opaque to microwaves which reduces the number of contributions to the reflected and backscattered components from the air-ice and air-snow surfaces.

Another important element during the melt season is the occurrence of melting and freezing temperatures within a short period of time. The development of a wet film on surfaces followed by newly formed crystals when the temperature drops offer conditions that translate into drastically different SAR images. We present in this paper two images recorded a few days apart that demonstrate that ridge extraction could be better achieved on images recorded late in the afternoon.

Pressure ridge detection relies on enhanced signal backscattered from tilted surfaces. Modelling an IFOV as an ensemble of ice blocks, the probability that one of them will be oriented with a face almost normal to the incident beam is a function of the number of blocks in the area. Therefore, the smaller the blocks in a ridge, the higher is the probability that a pixel will be extracted as a ridge pixel. Actually, our results show that below a certain size, the intensification of the signal provided by a single block is not sufficient to allow a pixel to be classified as a ridge pixel. It results that depending on the size of blocks, a ridge may be more or less clearly defined on an image. It follows that applying a set of threshold could be used to obtain more information on the size of ice blocks in ridges.

ACKNOWLEDGEMENTS

We thank D. Barber for his constructive comments on the probabilistic model. This work was made possible by funding from NSERC.

REFERENCES

1 Hudier E, C Fuentes & P Larouche,1999. Extraction des crêtes de pression sur image radarsat en mode fin. In: Fourth International Airborne Remote Sensing Conference and Exhibition/ 21st Canadian Symposium on Remote Sensing (Ottawa, Ontario, Canada, 21-24 June 1999)

2 Lytle V I & S F Ackley, 1991. Sea ice ridging in the eastern Weddell sea. Journal of Geophysical Research, 96: 18411-18416

3 Similä M, 1991. Statistical description of sea ice ridging intensity by SAR imagery. In: Proceeding of the 11th Annual Int. Geosc. and Remote Sensing Symp., Vol.3 (Espoo, Finland, June 3-6 1991) 1223-1227

4 Wadhams P, 1984. Sea ice morphology and its measurements. In: Arctic Technology and Policy, edited by I Dyer and C Chryssostomidis (Hemisphere Publishing Corporation, Washington DC) 179-195

5 Williams E, C W M Swithinbank & G deQ Robin, 1975. A submarine study of Arctic pack ice. Journal of Glaciology, 15: 349-362

6 Gow A J & W B Tucker III, 1990. Sea ice in the polar region. In: Polar Oceanography, Part A, edited by W O Smith Jr (Academic Press, San Diego) 47-122

7 Wadhams P, 1992. Sea ice thickness distribution in the Greenland sea and Eurasian Basin May 1987. Journal of Geophysical Research, C4: 5331-5348

8 Omsted A & J S Wetlaufer, 1992. Ice growth and oceanic heat flux; models and measurements. Journal of Geophysical Research, 97: 9383-9390

9 Onstott R G, 1992. SAR and Scatterometer signatures of sea ice. In: Microwave Remote Sensing of Sea Ice, chapter 5, edited by F D Carsey, Geophys. Monog. 68 (American Geophysical Union, Washington, DC) 73-104

10 Dierking W, H Skriver & P Gudmandsen, 2003. SAR Polarimetry for sea ice classification. Workshop on Application of SAR Polarimetry and Polarimetric Interferometry (ESA-ESRIN, Frascati, Italy) 10 pp.

11 Ulaby F T, R Moore & A Fung, 1986. Microwave Remote Sensing, Active and Passive, Vol. 3. (Addison Wesley, Reading)

12 Guneriussen T, 1997. Backscattering properties of a wet snow cover derived from ERS-1 SAR data. International Journal of Remote Sensing, 18(2): 375-392

13 Oh Y, K Sarabandi & F T Ulaby, 1992. An empirical model and an inversion technique for radar scattering from bare soil surfaces. IEEE Transactions on Geoscience and Remote Sensing, 30: 370-382

14 Shi J & J Dozier, 1995. Inferring snow wetness using C-band data from SIR-C's polarimetric Symphetic Aperture Radar. IEEE Transactions on Geoscience and Remote Sensing, 33(4): 905-914

15 Manninen A T, 1997. Surface roughness of Baltic sea ice. Journal of Geophysical Research, 102: 1119-1139

16 Ulaby F T & C Elachi, 1990. Radar Polarimetry for Geoscience Applications (Artech House Inc.)

17 Boerner W M, H Mott, E Luneburg, C Livingstone, B Brisco, R J Brown & J S Paterson, 1998. Polarimetry in radar remote sensing : basic and applied concepts. In: Principles and Applications of Imaging Radar, chapter 5, edited by Henderson and Lewis (Wiley & Sons) 271-358

18 Ulaby FT, F Kouyate, A K Fung & A G Sieber, 1982. Backscattering model for a randomly perturbed periodic surface. IEEE Transactions on Geoscience and Remote Sensing, GE-20: 518-528

19 Fung A K, 1994. Microwave Scattering and Emission Models and their Applications (Artech House, Norwood, MA)

20 Fung A K & H J Eom, 1983. Coherent scattering of a spherical wave from an irregular surface. IEEE Transactions on Antennas and Propagation, AP-31(1): 68-72

21 Davenport W B & W L Root, 1958. An Introduction to the Theory of Random Signals and Noise (McGraw-Hill Book Company, New York)

22 Kim Y S, 1984. Theoretical and Experimental Study of Radar Backscatter from Sea Ice. PhD. Dissertation (University of Kansas, Lawrence, Kansas)

23 Kim Y S, R K Moore & R G Onstott, 1984. Theoretical and experimental study of radar backscatter from sea ice. Remote Sensing Laboratory, Univ. Kansas Report (Kansas, U.S.A.) RSL TR 331-337

24 Hudier E, 2000. Pressure ridges extraction using Radarsat fine beam mode. In: Remote Sensing in the 21st Century: Economic and Environmental Applications, edited by J L Casanova (Balkema, Rotterdam) 467-473